Imaging performance of a LaBr3:Ce scintillation detector for photon counting x-ray computed tomography

Simulation study

Taguchi, Katsuyuki; Schaart, Dennis R.; Goorden, Marlies C.; Hsieh, Scott S.

DOI
10.1002/mp.17436

Publication date
2025

Document Version
Final published version

Published in
Medical Physics

Citation (APA)
Taguchi, K., Schaart, D. R., Goorden, M. C., & Hsieh, S. S. (2025). Imaging performance of a LaBr3:Ce scintillation detector for photon counting x-ray computed tomography: Simulation study. *Medical Physics*, *52*(1), 158-170. https://doi.org/10.1002/mp.17436

Received: 12 June 2024 | Revised: 11 September 2024 | Accepted: 12 September 2024

DOI: 10.1002/mp.17436

RESEARCH ARTICLE

MEDICAL PHYSICS

Imaging performance of a $LaBr_3$:Ce scintillation detector for photon counting x-ray computed tomography: Simulation study

Katsuyuki Taguchi[1] | **Dennis R. Schaart**[2] | **Marlies C. Goorden**[2] | **Scott S. Hsieh**[3]

[1]The Russell H. Morgan Department of Radiology and Radiological Science, Johns Hopkins University School of Medicine, Baltimore, Maryland, USA

[2]Department of Radiation Science and Technology, Delft University of Technology, Delft, The Netherlands

[3]Department of Radiology, May Clinic, Rochester, Minnesota, USA

Correspondence
Katsuyuki Taguchi, 601 North Caroline Street, JHOC 4267, Baltimore, MD 21287, USA.
Email: ktaguchi@jhmi.edu

Funding information
National Institute of Biomedical Imaging and Bioengineering of National Institutes of Health, Grant/Award Numbers: R21 EB029739, R01 EB035553; European Union under the grant agreement, Grant/Award Number: 101112053

Abstract

Background: Photon counting detectors (PCDs) for x-ray computed tomography (CT) are the future of CT imaging. At present, semiconductor-based PCDs such as cadmium telluride (CdTe), cadmium zinc telluride, and silicon have been either used or investigated for clinical PCD CT. Unfortunately, all of them have the same major challenges, namely high cost and limited spectral signal-to-noise ratio (SNR). Recent studies showed that some high-quality scintillators, such as lanthanum bromide doped with cerium ($LaBr_3$:Ce), are less expensive and almost as fast as CdTe.

Purpose: The objective of this study is to assess the performance of a $LaBr_3$:Ce PCD for clinical x-ray CT.

Methods: We performed Monte Carlo simulations and compared the performance of 3 mm thick $LaBr_3$:Ce and 2 mm thick CdTe for PCD CT with x-rays at 120 kVp and 20–1000 mA. The two PCDs were operated with either a threshold–subtract (TS) counting scheme or a direct energy binning (DB) counting scheme. The performance was assessed in terms of the accuracy of registered spectra, counting capability, and count-rate-dependent spectral imaging-task performance, for conventional CT imaging, water–bone material decomposition, and K-edge imaging with tungsten as the K-edge material. The performance for these imaging-tasks was quantified by nCRLB, that is, the Cramér–Rao lower bound on the variance of basis line-integral estimation, normalized by the corresponding value of CdTe at 20 mA.

Results: The spectrum recorded by CdTe was distorted significantly due to charge sharing, whereas the spectra recorded by $LaBr_3$:Ce better matched the incident spectrum. The dead time, estimated by fitting a paralyzable detector model to the count-rate curves, was 20.7, 15.0, 37.2, and 13.0 ns for CdTe with TS, CdTe with DB, $LaBr_3$:Ce with TS, and $LaBr_3$:Ce with DB, respectively. Conventional CT imaging showed an adverse effect of reduced geometrical efficiency due to optical reflectors in $LaBr_3$:Ce PCD. The nCRLBs (a lower value indicates a better SNR) for CdTe with TS, CdTe with DB, $LaBr_3$:Ce with TS, $LaBr_3$:Ce with DB, and the ideal PCD, were 1.00 ± 0.01, 1.00 ± 0.01, 1.18 ± 0.02, 1.18 ± 0.02, and 0.79 ± 0.01, respectively, at 20 mA. The nCRLBs for water–bone material decomposition, in the same order, were 1.00 ± 0.02, 1.00 ± 0.02, 0.85 ± 0.02, 0.85 ± 0.02, and 0.24 ± 0.02, respectively, at 20 mA; and 0.98 ± 0.02, 0.98 ± 0.02, 1.09 ± 0.02, 0.83 ± 0.02, and 0.24 ± 0.02, respectively, at 1000 mA. Finally, the nCRLBs for K-edge imaging, the most demanding task among the five, were 1.00 ± 0.02, 1.00 ± 0.02, 0.55 ± 0.02, 0.55 ± 0.02, and 0.13 ± 0.02, respectively, at 20 mA; and 2.45 ± 0.02, 2.29 ± 0.02, 3.12 ± 0.02, 2.11 ± 0.02, and 0.13 ± 0.02, respectively, at 1,000 mA.

Conclusion: The Monte Carlo simulations showed that, compared to CdTe with either TS or DB, $LaBr_3$:Ce with DB provided more accurate spectra, comparable or better counting capability, and superior spectral imaging-task performances, that is, water–bone material decomposition and K-edge imaging. CdTe had a better performance than $LaBr_3$:Ce for the conventional CT imaging task due to its higher geometrical efficiency. $LaBr_3$:Ce PCD with DB scheme may be an excellent alternative option for CdTe PCD.

KEYWORDS
computed tomography, photon counting detector, scintillator

1 | INTRODUCTION

X-ray computed tomography (CT) scanners are presently undergoing the largest architectural change since the introduction of multidetector-row CT (or MDCT) 26 years ago: they are moving from energy-integrating detectors (EIDs) to photon-counting detectors (PCDs).[1–4] PCDs offer three times the spatial resolution of previous EIDs at lower noise level or lower radiation dose, and also provide retrospective spectral imaging.[5–7] Today, two PCD CT scanners are approved for sale,[4,5] and three others have advanced to human imaging experiments.[8–11] The community was quickly impressed with 0.2 mm high-resolution CT images enabled by PCD CT, while high-resolution spectral imaging has also been finding applications, including iodine maps, virtual non-contrast images, and accurate thrombus/lumen images with no blooming or partial volume artifact.

The consensus in the CT community is that this is just the beginning of the PCD CT era. It is foreseen that its performance will further improve, and that PCD CT will come down to mid- and low-tier market segments over the next decade. In other words, PCD CT systems will become workhorse scanners in the healthcare system soon. The reason for this expectation is simple: PCD CT systems will be as easy to use as older single-energy CT systems, which fits the users' profile in general community hospitals and imaging centers. Artificial intelligence (AI) software on the reading workstation or application specialists working at imaging servers will process spectral CT data and report findings.

There are two major issues current PCD CT faces, the cost and the poor signal-to-noise ratio (SNR) of spectral images. Both types of PCD CT being developed and studied by CT vendors, that is, face-on cadmium telluride (CdTe) (or cadmium zinc telluride, CZT) PCD CT[1] and edge-on silicon PCD CT,[12] have these issues as outlined below.

1.1 | Cost

High-purity CdTe crystals are very expensive to manufacture, as the production yield is low. We expect a cost reduction over time, but this may be at a slow pace. The sheer volume required and special material processing make silicon PCDs as expensive as CdTe PCDs. Silicon is lighter than CdTe and thus needs to be made 30 times thicker to have comparable x-ray stopping power. This 30-fold volume increase offsets the lower price per unit volume. In addition, a clinical silicon PCD needs high-quality silicon crystals, which is significantly more expensive than off-the-shelf crystals.

1.2 | Spectral SNR

Both CdTe and silicon are direct-conversion detectors, meaning that they measure the number of photons and their energies by converting an x-ray photon directly into a charge cloud. The noise of the spectral signals is determined by the following factors related to detection physics: (a) dead space (or geometrical efficiency), (b) stopping power (or detection efficiency), (c) charge sharing and x-ray crosstalk between PCD pixels, and (d) pulse pileup (causing x-ray flux-dependent distortion of the photon count and spectral information). Due to these factors, the noise of current CdTe PCD CT is significantly larger than it would be with ideal detectors. Previous studies estimated that the noise standard deviation was increased 1.6-fold for iodine imaging[13] (96 percent-points/61 percent-points = 1.6, Table II, PC realistic/ideal, 4 bins) or 2.7-fold for K-edge imaging[14] ($\sqrt{8.43/1.14} = 2.7$, Table III, boxcar, 225 μm, 4 bins). We will show similar results in Section 3.3. Charge sharing is particularly harmful in this respect. It refers to the effect that the charge cloud generated by the x-ray can be split between adjacent pixels. This distorts the spectrum and increases noise, because the noise variance of double-counted photons is four times as large as that of the original data. [Note: $Var(2X) = 2^2 E(X)$ with X being a Poisson random variable.] Edge-on silicon effectively reduces pulse pileup, but silicon has poor energy sensitivity because little spectral signal remains after energy-insensitive Compton scattering. A Monte Carlo (MC) simulation estimated that its frequency-dependent detective quantum efficiency [DQE(f)] was only 12%–41% of CdTe at 80 keV. Another study

estimated a zero-frequency DQE, DQE(0), to be 5%−29% worse than CdTe.[15]

We believe that both of these problems—the cost and the poor spectral SNR—can be addressed by using an old but new technology: scintillators. Scintillators are inexpensive in general and are commonly used in energy integrating CT detectors (EIDs), but were long thought to be too slow to count individual photons and resolve their energies as is done in PCDs. Recent experimental studies showed that modern scintillators such as lanthanum bromide doped with cerium ($LaBr_3$:Ce) can be very fast, in fact, almost as fast as CdTe.[16,17] While the basic characteristics of $LaBr_3$:Ce have been studied well in the past,[18–21] the material has successfully been implemented in medical imaging detectors,[22–25] and the cost is expected to be 10%−15% of those of CdTe or CZT, its potential as a CT detector has not yet been investigated thoroughly. Thus, the aim of this study is to investigate the potential of a $LaBr_3$:Ce PCD for clinical PCD CT.

The structure of this article is as follows. In Section 2, we outline MC simulation methods and performance evaluation schemes used. We present results in Section 3, discuss relevant issues in Section 4, and conclude the article in Section 5.

2 | METHODS

In this section, we outline the $LaBr_3$:Ce PCD, the MC simulation method, and the performance evaluation schemes.

2.1 | Scintillator-based photon counting detector

We use $LaBr_3$:Ce with silicon photomultiplier (SiPM) readout to describe a scintillator-based PCD in general. Figure 1 presents the side and top views of the simulated $LaBr_3$:Ce and face-on CdTe PCDs. Both the $LaBr_3$:Ce and the CdTe PCD had 3 × 3 pixels within an aperture of (1 mm),[2] created by two-dimensional (2-D) anti-scatter grids (ASGs), which isolated the 3 × 3 pixels from the other pixels. The $LaBr_3$:Ce PCD had a pixel size of (300 μm),[2] a thickness of 3.0 mm, and optical reflection layers (optical septa) with a thickness of 50 μm in between adjacent pixels. It is noted that scintillator arrays with comparable or even smaller pixel sizes and reflector thicknesses have successfully been developed by various groups.[26–29] $LaBr_3$:Ce has a density of 5.06 g/cm^3 and a scintillation decay time constant of 16 ns.[30] The SiPM recharge time constant was set at 7.0 ns, matching the value of the SiPMs used in recent experiments with a prototype single-pixel $LaBr_3$:Ce PCD.[17] In first-order approximation, both the scintillation photon emission function and the single-photon signal of the SiPM can be described as exponential decay functions.[30] The expected pulse shape of the $LaBr_3$:Ce PCD then equals the convolution of these two functions, that is, a double-exponential pulse [Equation (1)] with a duration of 26.0 ns full-width-at-half-maximum (FWHM) and 56.0 ns full-width-at-tenth-maximum (FWTM) (Figure 2a).

$$f(t) = \frac{1}{\tau_{decay} - \tau_{recharge}} \left[exp\left(-\frac{t}{\tau_{decay}}\right) - exp\left(-\frac{t}{\tau_{recharge}}\right)\right], \quad (1)$$

where τ_{decay} and $\tau_{recharge}$ are the decay and recharge time constants discussed above.

The CdTe PCD had a pixel size of (333 μm),[2] a thickness of 2.0 mm (Figure 1), a density of 5.85 g/cm^3, and a 3-D Gaussian-distributed charge cloud with a FWHM of 72 μm.[31] The CdTe PCD had a slightly asymmetric monopolar pulse shape with a pulse duration of 14.0 ns FWHM and 25.0 ns FWTM,[32,33] which was created by connecting two normalized Gaussian functions at the peak (Figure 2a); the Gaussian parameters (i.e., the standard deviations) were 4.8 ns for the rising part of the pulse and 6.9 ns for the falling part. The FWHM and FWTM of the $LaBr_3$:Ce PCD pulses were 1.86 and 2.24 times longer, respectively, than those of the CdTe PCD. With the chosen thicknesses, the energy-dependent detection efficiencies of $LaBr_3$:Ce and CdTe were very close to each other (Figure 2b), if the detection efficiency is defined as the probability of interaction after an x-ray photon enters into the conversion material (i.e., not taking into account the influence of the optical reflectors and ASGs).

We briefly outline the detection process of a scintillator-based PCD. An x-ray photon interacts with a $LaBr_3$:Ce crystal via either the photoelectric effect or Compton scattering, with the photoelectric effect being dominant. The conditional yield of K-shell fluorescence x-rays is substantial, and the K-fluorescence x-ray either escapes from the PCD entirely or is absorbed by a PCD pixel (which is either the original/primary pixel or a neighbor/secondary pixel). With the energies of K_α and K_β of lanthanum (La) being 33.0−37.8 keV, the mean travel distance of La-K-fluoroscence x-ray is 223 μm in $LaBr_3$:Ce. When it is detected by one of the neighbor pixels, it results in crosstalk between the pixels, which we will denote by x-ray crosstalk in this article. Overall, $LaBr_3$:Ce has more x-ray crosstalk than CdTe, as the mean travel distances of Cd-K and Te-K-fluorescent x-rays are 124.4 and 61.6 μm, respectively.[1] When x-ray energy is deposited in $LaBr_3$:Ce, scintillation photons are emitted isotropically from the interaction site. They are reflected by the optical septa and finally detected by the SiPM underneath the scintillator pixel. The number

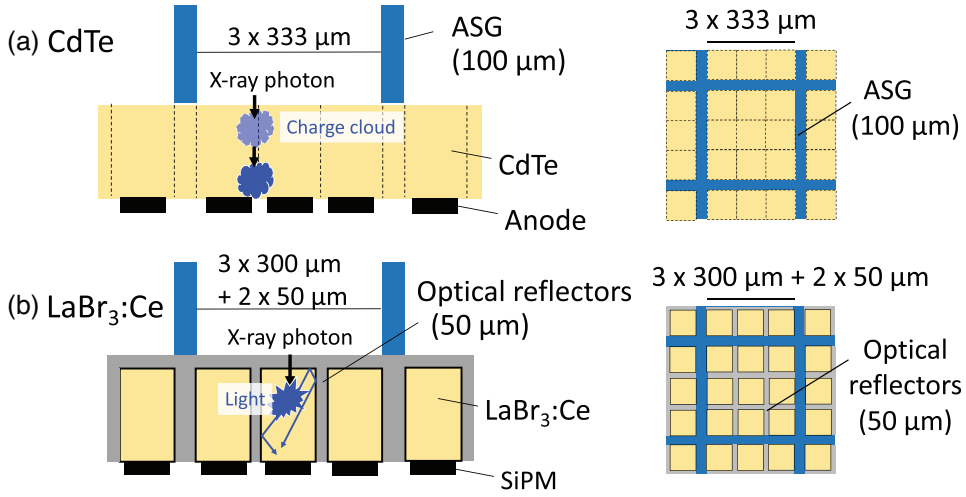

FIGURE 1 Side and top views of (a) the CdTe PCD and (b) the $LaBr_3$:Ce PCD used in this study. The thicknesses were 2.0 mm for the CdTe PCD and 3.0 mm for the $LaBr_3$:Ce PCD.

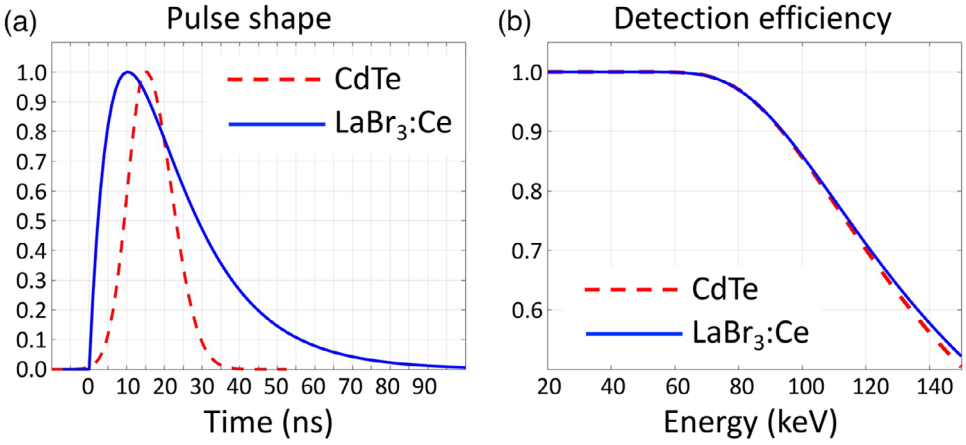

FIGURE 2 (a) Pulse shapes and (b) detection efficiency of 3.0 mm thick $LaBr_3$:Ce and 2.0 mm thick CdTe. The FWHM/FWTM of the pulse was 26 ns/56 ns for $LaBr_3$:Ce and 14 ns/25 ns for CdTe.

of scintillation photons is expected to be proportional to the deposited x-ray energy, but it is stochastic, resulting in a relatively broad photo-peak at the deposited energy (the FWHM-over-mean ratio commonly being referred to as the scintillator energy resolution). During the light reflection and detection, some light may leak into the neighbor pixels, which is called optical crosstalk. Note that in contrast with a CdTe PCD, there is no charge sharing during this photon detection process. Moreover, the noise of the readout electronics can easily be kept at a negligible level due to the internal gain of the SiPMs (typically in the order of 10^5, allowing a SiPM to detect single optical photons).[30] Thus, the output of each SiPM is an amplified analog pulse train, which can essentially be fed straight into a pulse height analysis (PHA) circuit, similar to that used with a CdTe PCD, but without need for a low-noise charge-sensitive amplifier and pulse shaping circuitry. For completion, it is noted that SiPMs produce so-called dark counts.[30] These are randomly occurring pulses, equal in shape and size to those produced by single optical photons. SiPM dark counts will not contribute to the registered photon count, as they stay below the minimum energy threshold typically used in a PCD. Moreover, since the dark count rate of a $(300\ \mu m)^2$ SiPM is expected to be in the order of 10 kHz, the probability for a dark count to occur during a 56 ns FWTM $LaBr_3$:Ce pulse is $< 10^{-3}$, so the influence on the registered x-ray energies can also be considered negligible.

2.2 | MC simulator and general settings

We modified the MC simulation program developed for and validated by a previous study,[33] which cascaded the following eight processes (1)–(8) that included three

temporal elements for CdTe PCD. The processes were (1) photon generation with randomized energies and time intervals based on a Poisson distribution, (2) photon interaction with the detector materials, (3) charge sharing and x-ray crosstalk (i.e., fluorescence x-ray emission and its re-absorption), based on a randomized incident location, interaction, and detection processes, (4) stochastic energy conversion for the scintillation process, (5) optical crosstalk with four neighbor pixels for the scintillator PCD, (6) stochastic and position-dependent signal arrival time delays, (7) pulse train generations with electronic noise, and (8) comparator detection signal generation with a rising pulse crossing energy thresholds. The sampling period of the modeled pulse trains was 1 ns. How these eight processes were performed for each PCD is outlined in Appendix A.

Two detection schemes with PHA were employed for (8): a threshold–subtract (TS) counting scheme[1,34–38] and a direct energy binning (DB) scheme.[39] The TS scheme is one of the most straightforward counting schemes; when a rising pulse crosses an energy threshold, it increments the corresponding counter. After a set time period, such as 200 μs, corresponding to a single view (projection) of the sinogram, the counters' data are read out and the output between adjacent energy thresholds are subtracted to compute the total number of pulse peaks that arrived within the two-sided energy bin. This scheme is known to have a risk of producing negative counts for energy bins, when the baseline is elevated with higher count-rates. See Appendix for more detail. The DB scheme directly counts the number of events that correspond to each energy window. The DB scheme is known for not having negative counts for any bins and making PCD faster (i.e., 34% shorter effective deadtime parameters and 59% higher maximum output count-rates). See Appendix B for more explanation of the DB scheme.

For the CdTe PCD, the MC program was run while skipping (4) and (5), and with charge arrival time delays due to interaction locations (both depth and pixel boundaries) and stochastic fluctuations for (6). Electronic noise with a standard deviation of 2.5 keV was added to the pulse train for (7).

For the $LaBr_3$:Ce PCD, the MC program was operated with a charge cloud size of 0.1 μm for (3) (which effectively eliminated charge sharing), deterministic and accurate arrival time for (6), and an electronic noise with a standard deviation of 0.1 keV for (7). Process (4) was modeled using a Gaussian distribution with the photopeak FWHM-to-mean ratio, $\mathrm{FWHM}(E)/E \times 100(\%)$, where E is the deposited energy, being equal to 15% FWHM at 60 keV and proportional to $1/\sqrt{E}$. The value of 15% FWHM at 60 keV was conservatively chosen as the average of the state-of-the-art energy resolution of 9.4% FWHM reported for $LaBr_3$:Ce at this energy[21] and the value of about 20% FWHM obtained by Van der Sar et al. in measurements with a single-pixel $LaBr_3$:Ce PCD,[17] in which the energy resolution was limited by the low (< 25%) photodetection efficiency of the SiPM and other experimental factors. As a first-order approximation of a high-quality scintillation crystal array, the optical crosstalk rate for (5) was set to 10% in total to the four closest neighbor pixels, and it was assumed that the leakage of deposited energy to these neighbors was distributed equally, hence 2.5% to each pixel. This approximation is justified if the number of scintillation photons is large, and the reflectivity of the optical septa between the pixels is high and uniform. Under these conditions, the scintillation photons will undergo a large number of reflections on average before either reaching the SiPM at the bottom of a high-aspect ratio pixel or crossing over to a neighbor pixel, resulting in an even distribution of optical crosstalk. We used Geant4[40] and recorded the spatial energy depositions of 5000 x-ray photons at a monoenergetic energy input, and repeated this with a 5-keV increment from 20 to 140 keV. The MC simulator stochastically used the 5000 samples with randomly sampled interaction locations and energies.

The following settings, which were similar to previous studies,[14,33,39] were used in this study unless otherwise noted. A 120-kVp x-ray spectrum with 2 mm aluminum and 10 cm water filter was generated by TASMICS/spektr[41,42] operated at 20−1000 mA. Both the $LaBr_3$:Ce PCD and CdTe PCD had four thresholds at 20, 45, 70, and 95 keV. The time window parameter for the DB scheme was set at 10 ns. A time duration per reading was varied to make the tube current–time product per reading constant at 2×10^{-2} mAs (e.g., 200 μs for 100 mA). X-rays were incident onto 3×3 pixels, but no x-rays were outside this area (including 2-D ASGs). A sum of 3×3 pixels was computed (which we call a super-pixel or macro-pixel in this paper) for each noise realization. A total of 10 000 noise realizations were performed for each mA setting.

2.3 | Performance evaluation schemes

2.3.1 | Spectra

The spectra of the $LaBr_3$:Ce PCD and the CdTe PCD for the central pixel of 3×3 pixels were assessed using (hypothetical) 26 energy bins with thresholds set at (5, 10, 15, 20, …, 130) keV. The tube current values were 50 , 400 , and 800 mA. The recorded spectra were normalized such that the area-under-the-curve above noise level E_n keV (= 17.5 keV) was set to 1. The incident spectrum was normalized such that the area-under-the-curve was set to 0.8, not 1, in order to take into account that fewer photons interacted with the PCDs due to limited detection efficiency and geometrical efficiency.

2.3.2 | Counting capabilities

Count-rate curves were obtained by the mean total counts per second (cps) per macro-pixel at 20 – 1000 mA. The probability of count was calculated by dividing the mean total number of counts at each tube current setting by that at 20 mA, assuming that the probability of count at 20 mA is very close to 1: $pr\ (TC) = y(TC)/y(20\ mA)$, where y is the total counts per reading and TC is the tube current setting. The effect of double-counting via charge sharing, if it occurs, is included in both of the data y.

The effective speed of the detector was derived from the count rate curves as follows. Using a paralyzable detector model,[43,44] the measured count-rate (cps/mm^2/mA) can be predicted as

$$y = (kI)\ exp\,(-kIS\tau)\,, \tag{2}$$

where τ is the deadtime of the PCD (s), which characterizes the speed of the PCD, k is the x-ray fluence rate incident onto either a CdTe or $LaBr_3$:Ce pixel (cps/mm^2/mA), I is the tube current (mA), and S is the detector pixel area (mm^2). The first two parameters, τ and k, are unique to each PCD and can be estimated by minimizing the difference between the measured and predicted count-rates:

$$\hat{\tau},\ \hat{k} = argmin_{\tau,k}\ \|\boldsymbol{y} - \tilde{\boldsymbol{y}}\|^2, \tag{3}$$

where $\boldsymbol{y}$ and $\tilde{\boldsymbol{y}}$ are vectors of the predicted and measured count-rates at various tube current values.

2.3.3 | Spectral imaging-task performances

Similar to our previous studies,[12,18,19] the performance of the PCDs was assessed by a non-spectral and two spectral imaging-tasks, that is, estimating the following basis line integrals: conventional CT imaging with water thickness estimation, water–bone material decomposition, and K-edge imaging with tungsten as part of water–bone–tungsten material decomposition. The target material for which the Cramér–Rao lower bound (CRLB) was computed as outlined below, was water, water (out of water and bone), and tungsten (out of water, bone, and tungsten) for the three imaging tasks, respectively. Although tungsten itself has not frequently been proposed as a contrast agent material for molecular CT imaging, its K-edge at 69.5 keV is intermediate between two other popular K-edge materials, gold (80.7 keV) and gadolinium (50.2 keV), hence tungsten can be considered a reasonable surrogate of these future agents.

Note that in image science, the word "task" (e.g., a task-specific assessment) is specifically used for clinical tasks that observers will perform using the obtained images, such as lesion detection and characterization (or classification and parameter estimation).[45] In this article, we use the term "imaging-task" to indicate the dimensionality of the imaging problem, that is, the number of parameters required to describe the content of a voxel accurately, thus supporting many clinical tasks. When a detector provides unbiased parameter estimates with minimum variances, an imaging system that uses such a detector is expected to perform well (i.e., with high dose efficiency) for many clinical tasks on the basis of the corresponding imaging-task (although there always will be exceptions).

Using the same procedure as in previous studies, the CRLB, which denotes the minimum variance achievable with unbiased estimation, was computed for each spectral imaging-task. Bootstrap resampling was performed 1000 times for each condition and the above process was performed for each bootstrap resample, producing 1000 CRLB values. The mean and the standard deviation of CRLB was computed over 1000 CRLB values, which were then normalized to the mean CRLB of the CdTe PCD at 20 mA for each spectral imaging-task to yield the normalized CRLB. In other words, all results were normalized to those obtained for the current state-of-the-art clinical PCD technology operating at near-zero pile-up conditions.

3 | RESULTS

3.1 | Spectrum

The $LaBr_3$:Ce spectra with TS and DB were identical at 50 mA and matched the incident spectrum better than the CdTe spectrum did (Figure 3a), with a distinct bump near 60 keV, where the characteristic x-rays of the tungsten anode are present, and fewer counts for energies < 35 keV. There was a distinct peak in the 30–45 keV energy range, which corresponded to fluorescence x-rays of lanthanum and constituted the major cause of x-ray crosstalk. In contrast, the spectrum recorded by CdTe was distorted significantly even though the pixel size was larger (333 vs. 300 μm), which would be expected to decrease charge sharing and improve the spectrum. The tungsten characteristic x-rays near 60 keV and fluorescence x-ray peak near 24–28 keV created only low and blurred bumps, and overall, the incident spectrum's shape was lost, with counts increasing monotonically toward lower energies.

Spectra of all of the four PCDs were distorted further as count-rates were increased to 400 and 800 mA (Figure 3b,c). Counts at lower energies (< 60 keV) were decreased, the bumps and peaks blurred, and counts at higher energies increased. These are typical effects of pulse pileup on recorded spectra. $LaBr_3$:Ce with

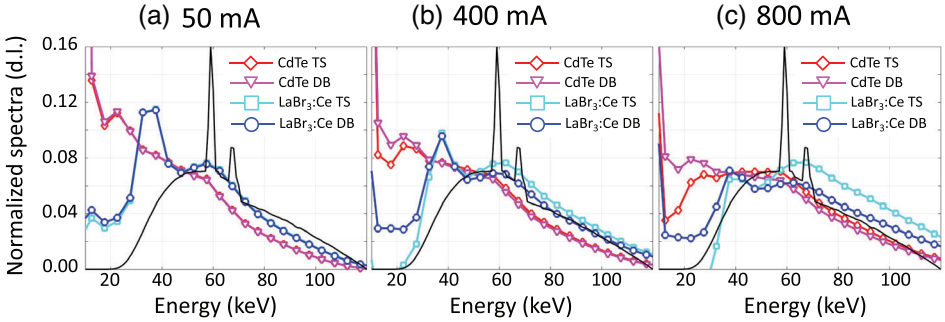

FIGURE 3 Recorded spectra of CdTe with TS, CdTe with DB, $LaBr_3$:Ce with TS, and $LaBr_3$:Ce with DB at (a) 50 mA, (b) 400 mA, and (c) 800 mA. The black curve is the incident spectrum.

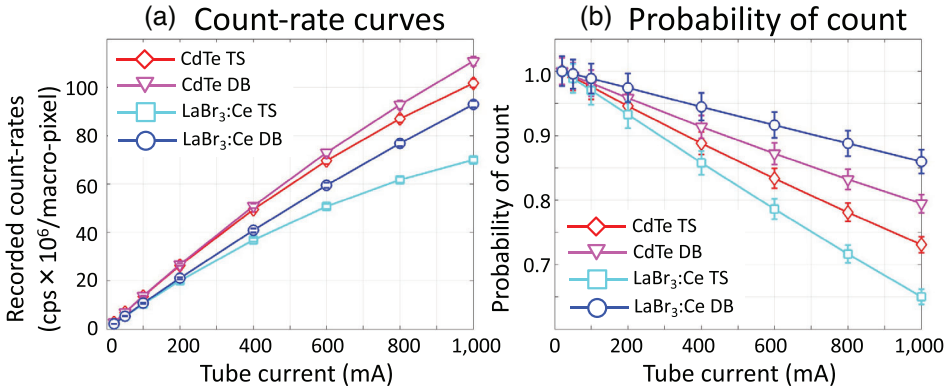

FIGURE 4 Counting capabilities of the four PCDs, based on CdTe or $LaBr_3$:Ce with either TS or DB scheme, (a) count-rate curves and (b) probabilities of count. The aperture area of for one macro-pixel between ASGs was 1.0 mm^2.

TS showed more drastic changes (i.e., stronger effects of pulse pileup) than $LaBr_3$:Ce with DB did, which is consistent with the counting capabilities and spectral imaging-task performances that will be presented in the following sections.

3.2 | Counting capabilities

Recorded count-rates of $LaBr_3$:Ce with TS were lower than those of CdTe with TS by 23%–32% for the same tube current setting (Figure 4a), whereas those of $LaBr_3$:Ce DB were still lower than, but closer to, those of CdTe, the differences being 9%–23%. We believe that these differences can be attributed to the different sensor areas, the different pulse durations (see Figure 2a and Section 2.1), and the absence/presence of charge sharing. The probability of count at 800 mA was 0.78, 0.86, 0.72, and 0.89 for CdTe with TS, CdTe with DB, $LaBr_3$:Ce with TS, and $LaBr_3$:Ce with DB, respectively (Figure 4b). The higher probability for $LaBr_3$:Ce with DB compared to $LaBr_3$:Ce with TS demonstrates the merit of the DB counting scheme. Note that due to the higher geometrical efficiency, CdTe observed higher incident photon count-rates than $LaBr_3$:Ce did at the same tube current. In addition, charge sharing increases pulse-rates observed at anodes. Both of them contributed to lower probabilities of count for CdTe. This point is further discussed in Discussion.

The estimated deadtime parameter τ was 20.7, 15.0, 37.2, and 13.0 ns for CdTe with TS, CdTe with DB, $LaBr_3$:Ce with TS, and $LaBr_3$:Ce with DB, respectively. Probably the most unexpected outcome was that the deadtime τ for $LaBr_3$:Ce with DB was 37% shorter than for CdTe with TS, and 13% shorter than CdTe with DB. Notice that τ represents the speed of detector and that the effect of pixel size (S) has been excluded [see Equations (1)–(2)]. The deadtime for $LaBr_3$:Ce with TS was 1.80(= 37.2/20.7) times longer than CdTe with TS, which is close to the ratio of FWHM's of their pulses (26.0/14.0 = 1.86). The improvement from $LaBr_3$:Ce with TS to $LaBr_3$:Ce with DB was as much as 65%, significantly more than the 28% improvement observed between CdTe with TS and CdTe with DB in this study (which is comparable to the 34% improvement found in a previous study[39]). We suspect that this can be attributed to the faster rising and slower falling times of the $LaBr_3$:Ce pulse, which we shall study further in

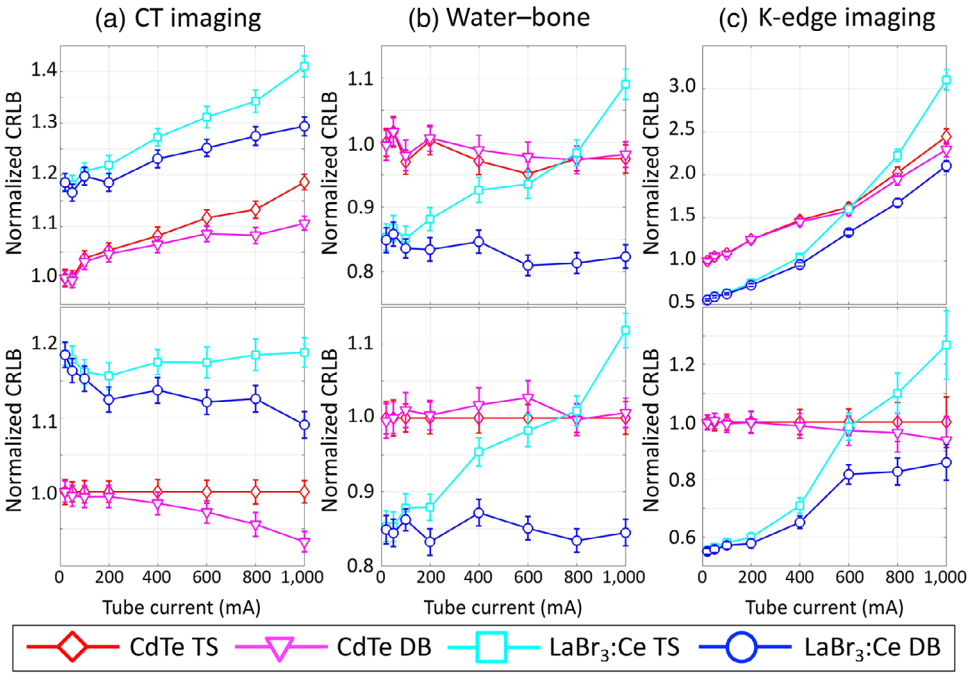

FIGURE 5 Spectral imaging-task performances of the four PCDs, based on CdTe or $LaBr_3$:Ce with either TS or DB scheme, for (a) conventional CT imaging, (b) water–bone material decomposition, and (c) K-edge imaging. Top row: CRLB values normalized to that of CdTe with TS at 20 mA. Bottom row: CRLB values normalized to those of CdTe with TS at the same tube currents. The normalized CRLBs for the ideal detector for the top row were 0.79 for CT imaging, 0.24 for water–bone material decomposition, and 0.13 for K-edge imaging. The corresponding values for the bottom row were 0.66–0.79 for CT imaging, 0.24–0.26 for water–bone material decomposition, and 0.05–0.13 for K-edge imaging.

future work. Overall, the counting capability of $LaBr_3$:Ce with DB was better than that of CdTe with TS and comparable to CdTe with DB.

3.3 | Spectral imaging-task performances

The normalized CRLB values for conventional CT imaging are presented in Figure 5a. We made the following four observations: (1) CRLB values increased for all of the four PCDs almost monotonically with increasing incident count-rate (i.e., tube current), presenting a straightforward effect of pileup on loss of counts, which degraded data statistics; (2) CRLBs of $LaBr_3$:Ce with TS were 16%–19% higher than those of CdTe with TS at the same mA setting (see Figure 5a, bottom), possibly mainly due to the difference in geometrical efficiency (which was 19% lower [i.e., $(300\ \mu m)^2$ / $(333\ \mu m)^2$ × 100% = 81%] and resulted in differences in the total number of incident photons that contributed to measured counts); (3) CRLB of $LaBr_3$:Ce with DB was identical to that of $LaBr_3$:Ce with TS at 20 mA; however, (4) CRLBs of $LaBr_3$:Ce with DB were less affected by count-rate than $LaBr_3$:Ce with TS and approached those of CdTe with increasing tube current. The difference from CdTe with TS was as small as 9% at 1000 mA.

The normalized CRLB values for the water–bone material decomposition are presented in Figure 5b. The observations included (5) CRLB values of both $LaBr_3$:Ce with TS and $LaBr_3$:Ce with DB at 20 mA were 15% lower than CdTe; (6) but CRLB values of $LaBr_3$:Ce with TS increased monotonically with increasing count-rate and crossed CdTe at ~750 mA; (7) in contrast, CRLB values of all of PCD except $LaBr_3$:Ce with TS were almost unaffected by the count-rate; and (8) CRLB values of $LaBr_3$:Ce with DB stayed better than CdTe by 13%–17% consistently (see Figure 5b, bottom). We believe that (5) can be attributed to the more accurate spectra of $LaBr_3$:Ce (see Figure 3) and that (6) and (8) are due to better counting capabilities, discussed in Section 3.2. The observation (7) might be surprising to some readers, but it is consistent with previous studies. See, for example, data with 1–500 mA, Table 2, Ref. 33, where probabilities of count with the TS scheme were 0.72–1.00 (Figure 6d, Ref. 33, which were comparable to our data for 20–1000 mA (probabilities for CdTe with TS were 0.73–1.00). The CRLB values for water–bone material decomposition seem to be less affected (relative to conventional CT imaging or K-edge imaging) until the probability of count goes below a certain level. In Ref. 33, the normalized CRLB increased from 1.06 to 1.24 when the probability decreased from 0.60 to 0.52.

The normalized CRLB values for K-edge imaging are presented in Figure 5c, and we learned that (9) CRLB

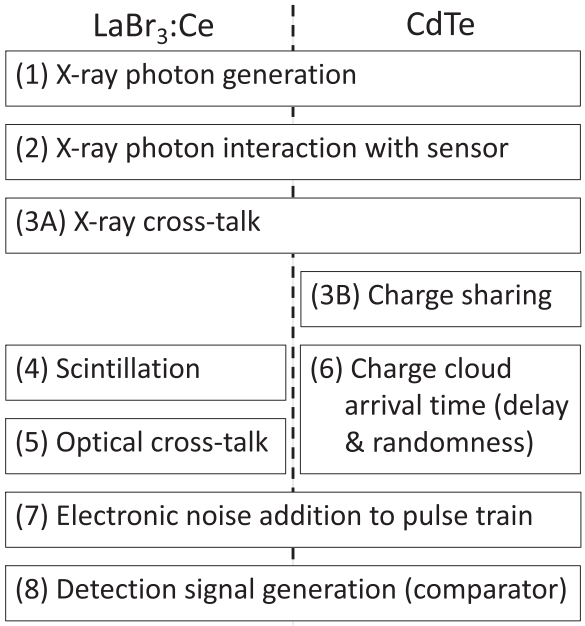

FIGURE 6 Processes (1)–(8) of the MC simulator (outlined in Section 2.2) included for CdTe PCD and LaBr3:Ce PCD, respectively.

values of all of PCDs increased monotonically with increasing incident count-rate due to pulse pileup; (10) CRLBs of both $LaBr_3$:Ce with TS and $LaBr_3$:Ce with DB were 45% lower than that of CdTe at 20 mA; (11) CRLB values of $LaBr_3$:Ce with TS increased monotonically with increasing count-rates and crossed CdTe at ~650 mA; and (12) CRLB values of $LaBr_3$:Ce with DB stayed better than CdTe with TS by 14%–45% (Figure 5c, bottom), although the advantages decreased with increasing count-rate.

4 | DISCUSSION

We simulated a realistic $LaBr_3$:Ce PCD with two counting schemes, threshold subtraction and direct binning, and compared it against CdTe PCDs with TS and DB schemes. On the one hand, the $LaBr_3$:Ce PCD had disadvantages over CdTe in having a lower geometrical efficiency (19% lower), longer pulse duration (86% longer FWHM; 26 vs. 14 ns), worse FWHM energy resolution, potential occurrence of optical crosstalk, and more x-ray crosstalk. On the other hand, the $LaBr_3$:Ce PCD had an important advantage in the absence of charge sharing.

This study showed that a $LaBr_3$:Ce PCD with DB scheme might be an excellent alternative option to a CdTe PCD with either TS or DB scheme. The counting capability of the $LaBr_3$:Ce PCD with DB was 37% better than the CdTe PCD with TS and 13% better than the CdTe PCD with DB. The effect of charge sharing, or the lack thereof in the $LaBr_3$:Ce PCD, almost single-handedly outweighed all of the above-mentioned disadvantages of the $LaBr_3$:Ce PCD for the two spectral imaging-tasks investigated. In contrast, the $LaBr_3$:Ce PCD had a worse performance than CdTe for the non-spectral, conventional CT imaging-task, due to its lower geometrical efficiency. The CRLB values of water–bone material decomposition and K-edge imaging for the $LaBr_3$:Ce PCD with DB were 13%–17% and 14%–45% better, respectively, than those for CdTe; the CRLB values of CT imaging for the $LaBr_3$:Ce PCD with DB were 9%–17% worse than CdTe.

We believe that the superior spectral performance of the $LaBr_3$:Ce PCD with DB can be attributed to the following four factors: (a) spectra were more accurate thanks to the absence of charge sharing, (b) pulse rates on the pulse train were lower due to the absence of charge sharing and lower geometrical efficiency, (c) the DB counting scheme made PCDs effectively faster and less affected by pulse pileup, and (d) optical crosstalk did not degrade the quality of the spectral information because leaked energies were below the lowest threshold energy (20 keV). Let us further discuss (b), because the impact of charge sharing on count-rates has rarely been discussed. Charge sharing (in CdTe) will increase effective pulse-rates at an anode because charge clouds produced by neighbor photons (i.e., photons incident onto neighbor pixels) will hit the anode and generate additional pulses. This increase in pulse-rate was significant, as much as 30%–40% in this study. In contrast, with no charge sharing, $LaBr_3$:Ce receives additional pulses from neighbor pixels only via x-ray crosstalk and optical crosstalk. $LaBr_3$:Ce had more x-ray crosstalk than CdTe, but the impact of x-ray crosstalk on the measured spectra was limited and local (near the K-fluorescence peak energy only). Optical crosstalk did not contribute to the counts measured above the lowest threshold energy (20 keV).

It will be of interest to study the performance of $LaBr_3$:Ce with smaller pixels and different optical reflection layers. It is expected that the geometrical efficiency will be lower and the performance will be decreased when the pixel size is made smaller. It is important to point out that the performance of CdTe will also degrade with smaller pixels, because there will be more charge sharing. We anticipate that the overall trend may stay the same as in this study: CdTe is better for non-spectral (conventional CT) imaging-task thanks to its better geometrical efficiency, but $LaBr_3$:Ce with DB is better for spectral imaging-tasks owing to the absence of charge sharing. We shall leave this to a future study.

It is desirable to improve the performance of scintillator-based PCDs in terms of a few aspects, such as the geometrical efficiency, the uncertainty of energy conversion via the scintillation process, and the pulse duration. The use of thinner optical septa would improve the geometrical efficiency. Allowing more optical crosstalk up to, for example, 20%, may not degrade the performance at low count-rates, as 20%

of 100 keV divided into 4 pixels will be still as low as 5 keV per pixel. The optical crosstalk may affect the performance at higher count-rates, however, as it adds uncertainty to recorded energies of succeeding photons for neighbor pixels. We shall leave this topic to future work as well.

There are a few other scintillators currently being investigated for PCD CT, including cerium-doped yttrium–gadolinium–aluminum–gallium garnet (YGAG), a scintillator composed of gadolinium–aluminum–gallium garnet (GAGG)/gadolinium–fine aluminum–gallate (GFAG), and $(BZA)_2PbBr_4$. Sato et al.[46] developed a table-top system for pre-clinical CT geometry using YGAG and demonstrated accurate density maps of basis functions (i.e., simultaneous imaging of gadolinium and iodine). Shimazoe et al.[29] used GAGG/GFAG coupled to a finely pixelated SiPM array. The detector had 10 × 10 pixels with a pixel size of $(200\ \mu m)^2$ and 50 μm optical reflection layer. These works showed very encouraging results for scintillator-based PCD CT in general. We believe that $LaBr_3$:Ce is more suitable for clinical CT because it is faster than YGAG and GAGG/GFAG. Decay time constants for the latter materials are in the range of 50−70 ns, whereas it is 16 ns for $LaBr_3$:Ce. $(BZA)_2PbBr_4$ is even faster than $LaBr_3$:Ce, having a decay time of 4.2 ns,[47] but is expected to have more x-ray crosstalk, as the K_α and K_β energies are higher (72.8−84.9 keV for Pb vs. 33.0−37.8 keV for La) and the density of $(BZA)_2PbBr_4$ is lower than that of $LaBr_3$:Ce (2.23 vs. 5.06 g/cm^3). Nonetheless, it will be of interest to study the spectral imaging-task performance of these scintillators.

In clinical practice, spectral and non-spectral imaging tasks will be performed jointly, and one image may be expected to serve more than one imaging task. CT scan protocols are determined for the main target use of images/data; spectral tasks are more dose-demanding than non-spectral tasks. Given the increasing importance of spectral discrimination in the utility of CT, it is possible that clinical focus will shift from non-spectral tasks to spectral tasks over the years. If so, then the advantage of materials like LaBr3:Ce that excel in spectral tasks may increase the value of CT systems in the future.

This study has four more limitations, in addition to those that have already been discussed above. First, it was a computer simulation, not a physical experiment. We plan to construct a prototype $LaBr_3$:Ce PCD and compare the performance against a CdTe PCD in the future. Second, it was assumed that optical crosstalk to neighboring pixels is distributed evenly. While this is a reasonable assumption in a high-quality pixel array (see Section 2.2), a more detailed model may be more appropriate if the crosstalk probability increases, for example, due to the use of thinner optical septa. The trade-off between x-ray detection efficiency (geometric fill factor) and optical crosstalk probability is an interesting topic for future studies. Third, the simulation lacks modeling of the nonlinear energy measurement with pulse pileup. The single-photon avalanche diodes in a SiPM will generate lower pulses when avalanches are triggered during their re-charging process. This has not been modeled in our simulation yet and will be a topic of future research. Fourth, we have assessed the CRLBs for one "object," with 10 cm water and 2 mm aluminum. Different objects, that is, different spectra and count-rates, may change the CRLB values; however, we expect the rank orders of different PCDs and methods to be consistent regardless of spectra. See some results in Roessl et al.[48]

5 | CONCLUSION

We have used MC simulations to compare the performance of a $LaBr_3$:Ce PCD against a CdTe PCD. $LaBr_3$:Ce with direct binning performed comparable to or better than CdTe with either threshold subtraction or direct binning in terms of counting capabilities. CdTe had the least noise for non-spectral, conventional CT imaging; however, $LaBr_3$:Ce with DB out-performed CdTe in terms of both the accuracy of the recorded spectra and the CRLB values for the spectral imaging-tasks investigated. $LaBr_3$:Ce with DB may be an excellent alternative to CdTe for clinical PCD CT.

ACKNOWLEDGMENTS

Part of the effort made for this publication was supported by the National Institute of Biomedical Imaging and Bioengineering of National Institutes of Health under R21 EB029739 and R01 EB035553. The content is solely the responsibility of the authors and does not necessarily represent the official view of the National Institutes of Health.

Part of the effort made by Dennis R. Schaart and Marlies C. Goorden was supported by the European Union under the grant agreement number 101112053 (IMAGIO project, supported by the Innovative Healthy Initiative Joint Undertaking). Views and opinions expressed are however those of the authors only and do not necessarily reflect those of the European Union or Innovative Health Initiative Joint Undertaking. Neither the European Union nor the granting authority can be held responsible for them.

CONFLICT OF INTEREST STATEMENT

The authors have no additional relevant conflict of interest to disclose. The Johns Hopkins University has filed a patent on the direct energy binning scheme on behalf of Katsuyuki Taguchi, PhD.

DATA AVAILABILITY STATEMENT

The simulation data presented in this article may be made available to interested readers upon request.

Please submit the corresponding author a written proposal for collaborative projects.

REFERENCES

1. Taguchi K, Iwanczyk JS. Vision 20/20: single photon counting x-ray detectors in medical imaging. *Med Phys*. 2013;40(10):100901.
2. Hsieh SS, Leng S, Rajendran K, Tao S, McCollough CH. Photon counting CT: clinical applications and future developments. *IEEE Trans Radiat Plasma Med Sci*. 2020;5(4):441-452.
3. Leng S, Bruesewitz M, Tao S, et al. Photon-counting detector CT: system design and clinical applications of an emerging technology. *RadioGraphics*. 2019;39(3):729-743.
4. Flohr, T., Ulzheimer, S., Petersilka, M. et al. Basic principles and clinical potential of photon-counting detector CT. *Chinese J Acad Radiol* 2020;3:19–34.
5. Gaillandre Y, Duhamel A, Flohr T, et al. Ultra-high resolution CT imaging of interstitial lung disease: impact of photon-counting CT in 112 patients. *Eur Radiol*. 2023;33(8):5528-5539. published online ahead of print 20230418.
6. Benson JC, Rajendran K, Lane JI, et al. A new Frontier in temporal bone imaging: photon-counting detector CT demonstrates superior visualization of critical anatomic structures at reduced radiation dose. *Am J Neuroradiol*. 2022;43(4):579-584. published online ahead of print 20220324.
7. Hagen F, Soschynski M, Weis M, et al. Photon-counting computed tomography—clinical application in oncological, cardiovascular, and pediatric radiology. *Rofo*. 2024;196(1):25-35. published online ahead of print 20231004.
8. Boccalini S, Mayard C, Lacombe H, et al. Ultra-high-resolution and K-edge imaging of prosthetic heart valves with spectral photon-counting CT: A phantom study. *Invest Radiol* 2024;59(8):589–598.
9. Si-Mohamed S, Thivolet A, Bonnot, PE, et al., Improved peritoneal cavity and abdominal organ imaging using a biphasic contrast agent protocol and spectral photon counting computed tomography K-edge imaging. *Invest Radiol* 2018;53(10):629–639.
10. Muenzel D, Bar-Ness D, Roessl E, et al. Spectral photon-counting CT: initial experience with dual–contrast agent K-Edge colonography. *Radiology*. 2016;283(3):160890. http://pubs.rsna.org/doi/abs/160810.161148/radiol.2016160890
11. Zhan X, Zhang R, Niu X, et al. Comprehensive evaluations of a prototype full field-of-view photon counting CT system through phantom studies. *Phys Med Biol*. 2023;68(17):175007.
12. Sundberg C, Danielsson M, Persson M. Compton coincidence in silicon photon-counting CT detectors. *J Med Imaging (Bellingham, Wash)*. 2022;9(1):013501. published online ahead of print 20220208.
13. Faby S, Kuchenbecker S, Sawall S, et al. Performance of today's dual energy CT and future multi energy CT in virtual non-contrast imaging and in iodine quantification: a simulation study. *Med Phys*. 2015;42(7):4349-4366.
14. Taguchi K. Assessment of multi-energy inter-pixel coincidence counter (MEICC) for charge sharing correction or compensation for photon counting detectors with Boxcar signals. *IEEE Trans Radiat Plasma Med Sci*. 2021;5(4):465-475.
15. Persson M, Wang A, Pelc N. Detective quantum efficiency of photon-counting CdTe and Si detectors for computed tomography: a simulation study. *J Med Imaging*. 2020;7(4):043501.
16. van der Sar SJ, Brunner SE, Schaart DR. Silicon photomultiplier-based scintillation detectors for photon-counting CT: a feasibility study. *Med Phys*. 2021;48(10):6324-6338. published online ahead of print 20210625.
17. van der Sar S, Leibold D, Brunner S, Schaart D. LaBr3:ce and silicon photomultipliers: towards the optimal scintillating photon-counting detector. 7th International Conference on Image Formation in X-Ray Computed Tomography. 2022;Proc SPIE 12304:123040A.
18. van Loef EVD, Dorenbos P, van Eijk CWE, Krämer K, Güdel HU. High-energy-resolution scintillator: ce activated LaBr. *Appl Phys Lett*. 2001;79:1573-1575.
19. Glodo J, Moses WW, Higgins WM, et al. Effects of Ce concentration on scintillation properties of LaBr3 : ce. *Ieee T Nucl Sci*. 2005;52(5):1805-1808.
20. van Dam HT, Seifert S, Drozdowski W, Dorenbos P, Schaart DR. Optical absorption length, scattering length, and refractive index of LaBr3:ce3+. *Ieee T Nucl Sci*. 2012;59(3):656-664.
21. Alekhin MS, de Haas JTM, Khodyuk IV, et al. Improvement of gamma-ray energy resolution of LaBr3:ce3+ scintillation detectors by Sr2+ and Ca2+ co-doping. *Appl Phys Lett*. 2013;102(16).
22. Daube-Witherspoon ME, Surti S, Perkins A, et al. The imaging performance of a LaBr3-based PET scanner. *Phys Med Biol*. 2010;55(1):45-64.
23. Seifert S, van Dam HT, Huizenga J, et al. Monolithic LaBr3:ce crystals on silicon photomultiplier arrays for time-of-flight positron emission tomography. *Phys Med Biol*. 2012;57:2219-2233.
24. Aldawood S, Thirolf PG, Miani A, et al. Development of a Compton camera for prompt-gamma medical imaging. *Radiat Phys Chem*. 2017;140:190-197.
25. Barrientos L, Borja-Lloret M, Etxebeste A, et al. Performance evaluation of MACACO II Compton camera. *Nucl Instrum Meth A*. 2021:1014.
26. Imai Y, Nukui M, Ishihara Y, et al. Development and performance evaluation of an experimental fine pitch detector multislice CT scanner. *Med Phys*. 2009;36(4):1120-1127.
27. Cherry SR, Qi J. High Resolution PET with 250 micrometer LSO Detectors and Adaptive Zoom. U.S. Report DOE/ER/64677; TRN: US1204359 (2012). https://www.osti.gov/biblio/1032741
28. Godinez F, Gong K, Zhou J, Judenhofer MS, Chaudhari AJ, Badawi RD. Development of an ultra high resolution PET scanner for imaging rodent paws: pawPET. *Ieee Trans Radiat Plasma Med Sci*. 2018;2(1):7-16.
29. Shimazoe K, Kim D, Hamdan M, et al. Scintillator–single-photon avalanche diode array-based energy resolving photon counting X-ray detector. *(preprint)*. 2024 doi:10.21203/rs.3.rs-4182321/v1
30. Schaart DR. Physics and technology of time-of-flight PET detectors. *Phys Med Biol*. 2021;66(9).
31. Hsieh SS. Coincidence counting for charge sharing compensation in spectroscopic photon counting detectors. *IEEE Trans Med Imaging*. 2020;39(3):678-687. published online ahead of print 2019/08/10.
32. Taguchi K, Polster C, Segars WP, Aygun N, Stierstorfer K. Model-based pulse pileup and charge sharing compensation for photon counting detectors: a simulation study. *Med Phys*. 2022;49(8):5038-5051.
33. Taguchi K, Iwanczyk JS. Assessment of multi-energy inter-pixel coincidence counters for photon-counting detectors at the presence of charge sharing and pulse pileup: a simulation study. *Med Phys*. 2021;48(9):4909-4925.
34. Ballabriga R, Alozy J, Bandi FN, et al. Photon counting detectors for X-ray imaging with emphasis on CT. *IEEE Trans Radiat Plasma Med Sci*. 2020;5(4):422-440.
35. Iwanczyk JS, Nygard E, Meirav O, et al. Photon counting energy dispersive detector arrays for X-ray imaging. *IEEE Trans Nucl Sci*. 2009;56(3):535-542.
36. Barber WC, Nygard E, Wessel JC, et al. Energy-resolved photon-counting x-ray imaging arrays for clinical K-edge CT. Nuclear Science Symposium and Medical Imaging Conference (NSS/MIC), 2011 IEEE; 23–29 Oct. 2011, 2011; Valencia, Spain.
37. Steadman R, Herrmann C, Mulhens O, et al. ChromAIX: a high-rate energy-resolving photon-counting ASIC for spectral computed tomography. Medical Imaging 2010: Physics of Medical Imaging; 2010; San Diego, California, USA.
38. Steadman R, Herrmann C, Livne A. ChromAIX2: a large area, high count-rate energy-resolving photon counting ASIC for a

spectral CT prototype. *Nucl Instruments Methods Phys Res A*. 2017;862:18-24.
39. Taguchi K, Hsieh SS. Direct energy binning for photon counting detectors: simulation study. *Med Phys*. 2024;51(1):70-79.
40. Agostinelli S, Allison J, Amako K, et al. Geant4—a simulation toolkit. *Nucl Instruments Methods Phys Res A*. 2003;506(3):250-303.
41. Boone JM, Seibert JA. An accurate method for computer-generating tungsten anode x-ray spectra from 30 to 140 kV. *Med Phys*. 1997;24(11):1661-1670.
42. Punnoose J, Xu J, Sisniega A, Zbijewski W, Siewerdsen JH. Technical Note: spektr 3.0—A computational tool for x-ray spectrum modeling and analysis. *Med Phys*. 2016;43(8Part1):4711-4717.
43. Knoll GF. *Radiation Detection and Measurement*. 4th ed. John F. Wiley and Sons; 2010.
44. Taguchi K, Zhang M, Frey EC, et al. Modeling the performance of a photon counting x-ray detector for CT: energy response and pulse pileup effects. *Med Phys*. 2011;38(2):1089-1102.
45. Barrett HH, Myers K. *Foundations of Image Science*. 1st ed. Wiley-Interscience; 2003.
46. Sato D, Arimoto M, Ishiguro A, et al. Multi-energy in-vivo imaging of multiple contrast agents in a mouse using MPPC-based photon-counting CT. *Nucl Instruments Methods Phys Res A*. 2024;1064:169337.
47. van Blaaderen JJ, van der Sar S, Onggo D, et al. (BZA)2PbBr4: a potential scintillator for photon-counting computed tomography detectors. *J Luminesc*. 2023;263:120012.
48. Roessl E, Brendel B, Engel K, Schlomka J, Thran A, Proksa R. Sensitivity of photon-counting based K-Edge imaging in X-ray computed tomography. *Med Imaging IEEE Trans*. 2011;30(9):1678-1690.

How to cite this article: Taguchi K, Schaart DR, Goorden MC, Hsieh SS. Imaging performance of a $LaBr_3$:Ce scintillation detector for photon counting x-ray computed tomography: Simulation study. *Med Phys*. 2024;1-13. https://doi.org/10.1002/mp.17436

APPENDIX A

Figure 6 outlines the corresponding subset of processes (1)–(8) in the MC simulator (Section 2.2) included for the CdTe PCD and LaBr3:Ce PCD, respectively.

APPENDIX B

Single photon counting circuitry diagrams of the TS and DB schemes[39] are shown in Figure B1a and B1c, respectively. Note that the only difference between TS and DB is that DB has additional NOT and AND logical operators that are used for direct energy binning. DB does not actively detect pulse peaks. Many active pulse peak detection schemes may be susceptible to electronic noise because they take a derivative of the pulse train and detect its zeros. Instead, DB uses up-crossing events as follows: Every up-crossing event starts a timer t_k for a threshold k. When t_k reaches a pre-determined time, T_{DB}, bin k checks the timer for a threshold (k+1), t_{k+1}. If t_{k+1} is active and non-zero, it indicates that the pulse has exceeded threshold (k+1), which in turn, means that the pulse does not belong to bin k. It then simply resets t_k to zero and moves on. If the t_{k+1} is *not* active, it means that the pulse peak belongs to bin k. It then adds one count to bin counter B_k, resets timer t_k, and waits for the next photon. DB thus is a very simple modification from TS. In this study, T_{DB} was set at 10 ns.

When pulse pileup is severe and the pulse shape has a finite width, the baseline may be elevated to above zero when a new pulse arrives. This baseline elevation and its fluctuation over time may result in unexpected measurements with TS such as a negative count as shown in Figure B1b. In contrast, DB always outputs non-negative counts that represent the number of pulse peaks for each energy bin (see Figure B1d). The performances of TS and DB and their agreement with statistical models are reported in Ref. 39

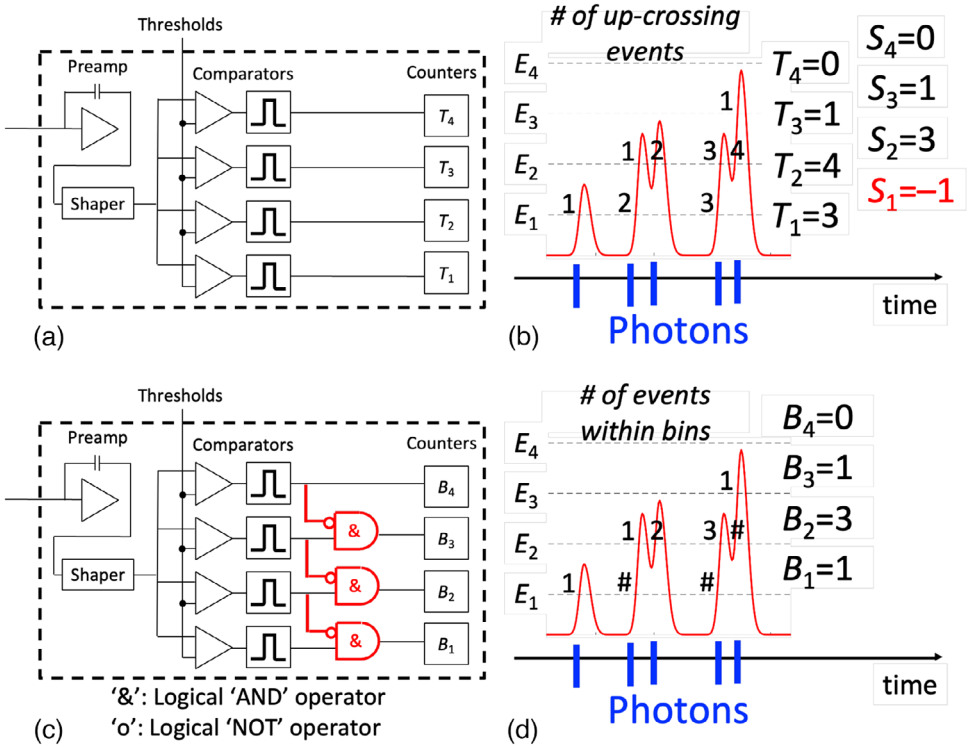

FIGURE B1 (a) A diagram of the TS scheme for one sub-pixel. (b) An example of pulse detection outcome using TS. Sequential up-crossings for each threshold are labeled with integers. (c) A diagram of the DB scheme for one sub-pixel. (d) An example of pulse detection outcome using DB. Up-crossings marked with "#" are not counted. Figure is from Ref. 39.